Article

On-The-Spot Sampling and Detection of Viral Particles on Solid Surfaces Using a Sponge Virus Sensor Incorporated with Finger-Press Fluid Release

Yang Tian and Liang Dong*

Cite This: https://doi.org/10.1021/acssensors.3c02766

Read Online

ACCESS | Metrics & More | Article Recommendations | SI Supporting Information

ABSTRACT: This paper presents a sponge-based electrochemical sensor for rapid, on-site collection and analysis of infectious viruses on solid surfaces. The device utilizes a conducting porous sponge modified with graphene, graphene oxide, and specific antibodies. The sponge serves as a hydrophilic porous electrode capable of liquid collection and electrochemical measurements. The device operation involves spraying an aqueous solution on a target surface, swiping the misted surface using the sponge, discharging an electrolyte solution with a simple finger press, and performing in situ incubation and electrochemical measurements. By leveraging the water-absorbing ability of the biofunctionalized conducting sponge, the sensor can effectively collect and quantify virus particles from the surface. The portability of the device is enhanced by introducing a push-release feature that dispenses the liquid electrolyte from a miniature reservoir onto the sensor surface. This reservoir has sharp edges to rupture a liquid sealing film with a finger press. The ability of the device to sample and quantify viral particles is demonstrated by using influenza A virus as the model. The sensor provided a calculated limit of detection of 0.4 TCID50/mL for H1N1 virus, along with a practical concentration range from $1-10^6$ TCID50/mL. Additionally, it achieves a 15% collection efficiency from single-run swiping on a tabletop surface. This versatile device allows for convenient on-site virus detection within minutes, eliminating the need for sample pretreatment and simplifying the entire sample collecting and measuring process. This device presents significant potential for rapid virus detection on solid surfaces.

KEYWORDS: virus sensor, electrochemical sensors, microfluidics, conducting polymer, graphene sponge
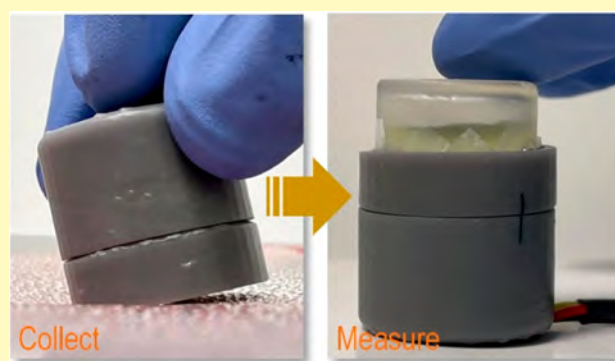
INTRODUCTION

The emergence of viral infections in respiratory diseases has significantly impacted both human health and porcine production. In the United States, a key example is the porcine reproductive and respiratory syndrome virus (PRRSV), which has led to increased productivity losses.[1] Similarly, influenza A virus (H1N1) has resulted in widespread human infections.[2] These respiratory viruses can become airborne and spread via aerosols generated by respiratory activities and can replicate and shed before symptoms become apparent.[3] Activities such as talking, coughing, or laughing can disperse aerosols, which can remain suspended in the air and then settle on surfaces.[4] Consequently, contact with these contaminated surfaces can lead to infections. Viral infections can also be transmitted through tainted food, water, and sewage, highlighting the need for timely virus surveillance and preventative strategies.[5]

While traditional virus diagnostic methods, such as reverse transcription-quantitative polymerase chain reaction (RT-qPCR),[6] enzyme-linked immunoassays (ELISA),[7] immuno-blotting,[8] and immunofluorescence assays,[9] are widely used for identifying various respiratory viruses, they have several limitations. The ELISA method, for example, requires costly and laborious antibody production, making large-scale use challenging.[10] Similarly, the RT-PCR method, while sensitive and specific, requires careful handling of RNA samples to prevent degradation, making it unsuitable for rapid on-site testing.[11] Furthermore, these traditional methods necessitate specialized equipment and highly trained personnel, escalating costs, and restricting accessibility. Therefore, there is an increasing need for rapid, affordable, and scalable diagnostic procedures for the on-site detection of respiratory viruses.

Portable virus sensors utilize a variety of approaches, such as optical,[12] electrochemical,[13] isothermal amplification,[14] micro-electromechanical-system,[15] giant magneto-resistive,[16] molec-
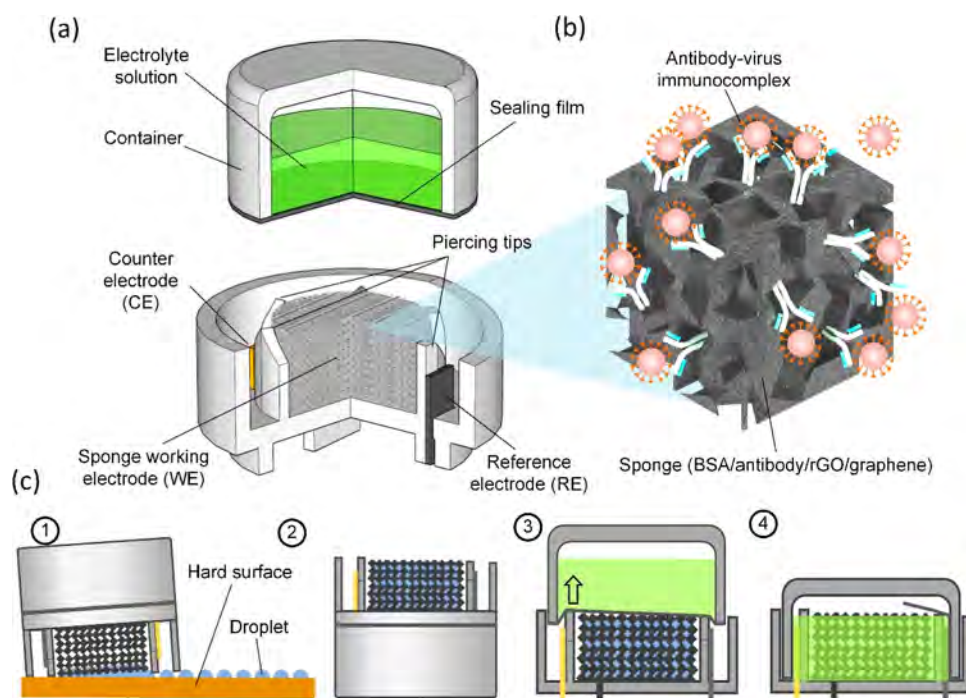
Figure 1. (a) Schematic of a portable virus sensor composed of a sponge-based electrochemical cell equipped with penetrating sharp edges. The cell is incorporated with a compact liquid reservoir holding a presealed electrolyte solution. (b) Diagram of the sponge electrode constructed from a silicone-based porous elastomer functionalized with graphene, reduced graphene oxide, and antibodies specific to the target virus. (c) Diagram of the device operational procedures that involve spraying an aqueous solution on the surface, swiping the misted surface with the sponge, releasing the electrolyte solution, and executing the incubation and detection of the virus within the electrochemical cell.

ularly imprinted polymer,[17] and paper-based microfluidic-based[18−21] methods, to detect viruses like influenza,[22] dengue,[23] SARS-CoV-2,[24] and Zika.[25] Among these methods, electrochemical sensors stand out for their high sensitivity and fast response and utilize specific interactions between viral particles and receptors such as antibodies and aptamers on sensing electrodes.[26] Surface modification with biofunctionalized materials such as silicon nanowires,[27] graphene,[28] carbon nanotubes,[29] quantum dots,[30] and many nanocomposites[31] are often incorporated to enhance the sensitivity of electrochemical sensors.

Different sampling technologies accompany virus detection methods to collect virus particles from diverse environments.[32,33] Devices like electrostatic air samplers,[34] bioaerosol cyclones,[35] and impingers[36] are used to collect airborne virus particles and other contaminants. Filtration and ultrafiltration are often employed for sampling viruses in water, while centrifugation can separate virus particles based on size and density.[37] Also, surface sampling typically involves sterile swabs,[38] cleaning cloth,[39] and tape-lift sampling.[40] Despite these advances, there has been a limited effort to integrate sampling and sensing into a device for on-site detection and surveillance of viruses that settle onto hard surfaces as aerosols.

This paper reports a portable electrochemical virus sensor that utilizes a conducting sponge-based platform for the rapid and specific detection of viruses on hard surfaces. The device can directly collect samples from the hard surface, dispense liquid electrolytes by a finger press, create specific antigen−antibody bonds on the surface of scaffolds, and conduct electrochemical measurements to quantify the target virus. The porous sponge can absorb water from the misted hard surface, transporting virus particles into the sponge. Upon contact with the interior surface of the sponge, the virus particles bind to

the biofunctionalized surface through the formation of antigen−antibody immunocomplexes. Moreover, a push-release mechanism is employed to discharge a presealed liquid electrolyte onto the sensor surface. The entire process, from moistening the hard surface to receiving results, takes several minutes. The effectiveness of the sensor is demonstrated using the swine H1N1 virus as a model, illustrating the potential of the sponge sensor for on-site sample collection and virus detection on hard surfaces.

■ SENSOR DESIGN

The device features a compact design for on-site sampling and analysis, making it a versatile solution for virus detection. The electrochemical cell consists of a hydrophilic conducting sponge as the working electrode (WE), a Ag/AgCl-based pseudo reference electrode (RE), and a thin-film gold (Au)-based counter electrode (CE) (Figure 1a). The sponge is modified with graphene, reduced graphene oxide (rGO), and specific antibodies targeting the virus of interest (Figure 1b). It is situated within a circular fence in the middle of the electrochemical cell. The porous structure of the sponge increases the loading capacity of the antibody molecules. These antibodies are immobilized on the surface of the sponge via the EDC-NHS chemistry method,[41] thereby enriching the interaction between the antibody and antigen of the target virus.

To collect viral samples from a solid surface, the surface is misted with a phosphate-buffered saline (PBS) solution (Figure 1c). The sponge then moved over the surface, drawing the liquid. A miniature liquid reservoir is designed to store the liquid electrolyte for the upcoming electrochemical measurement. It is sealed with a protective sealing film. The circular fence has sharp edges. A simple finger press against the sharp
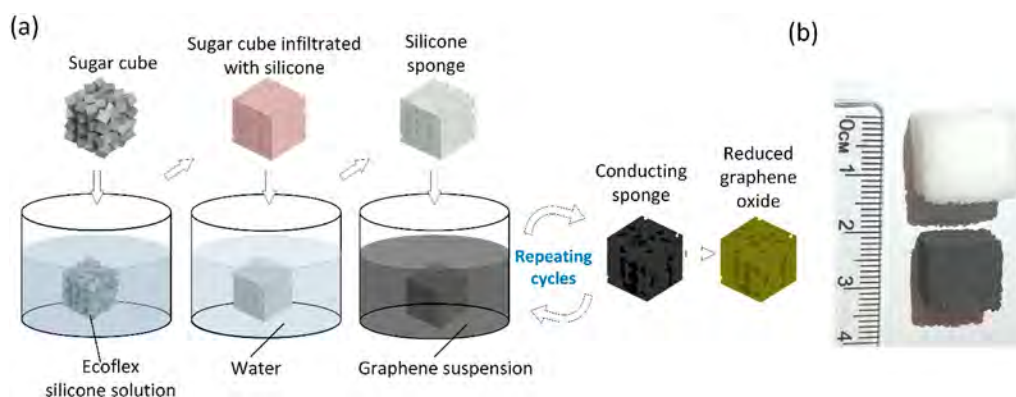
Figure 2. (a) Schematic of the fabrication process used to realize a silicone-based conducting sponge modified with graphene flakes and reduced graphene oxide. Sugar cubes served as templates to form the sponge. Repeated immersion in a graphene suspension followed by baking resulted in a conducting sponge. Further, drop casting of a suspension of reduced graphene oxide rendered the sponge hydrophilic properties. (b) Comparison of the size between the original silicone sponge and the sponge after the graphene flake and reduced graphene oxide treatment.

edges punctures the sealing film. Consequently, the electrolyte is discharged, immersing all the three electrodes of the sensor. The sensor is left still for a set duration, allowing for the bonding of antibodies and antigens.

■ EXPERIMENTAL SECTION

Materials. Silicone elastomer (Ecoflex 00−30) was purchased from Smooth-On, Inc. (Macungie, PA, USA). Sugar cubes (C&H Pure Cane) were acquired from Walmart. Bovine serum albumin (BSA), potassium chloride (KCl), and H1N1 antibodies (Anti-Swine H1N1 Hemagglutinin antibody produced in rabbit, SAB3500061) were purchased from Sigma-Aldrich (St. Louis MO, USA). Phosphate buffered saline (PBS), 1-ethyl-3-(3-(dimethylamino)propyl) carbodiimide hydrochloride (EDC), and N-hydroxysulfosuccinimide (NHS) were obtained from ThermoFisher Scientific (Waltham, MA, USA). Graphene dispersion (CGD-200 ML) was purchased from the Graphene Supermarket (Ronkonkoma, NY, USA), while potassium ferricyanide was sourced from Fisher Scientific (Pittsburgh, PA, USA). Reduced graphene oxide (rGO) was purchased from ACS Material (Pasadena, CA, USA). Fluorescein was purchased from ACROS Organics (CAS 2321-07-5) through Thermo Fisher Scientific (Waltham, MA, USA). Antiswine H1N1 Hemagglutinin antibodies were purchased from Sigma-Aldrich and are specific for the influenza A virus. These unconjugated antibodies were produced by the inoculation of rabbits and supplied in PBS with 0.02% sodium azide (an antimicrobial agent). The bulk antibody sample was aliquoted into smaller containers and stored at −20 °C for multiple uses. A single dose of antibodies was thawed and then transferred to an incubation tube during surface functionalization.

The swine IAV isolate A/swine/MO/A01203163/2012 (H1N1) was isolated, propagated, and titrated in MDCK cells (ATCC CCL-34) following a previously published protocol.[42] The IAV isolate stock demonstrated an infectious titer of 10^7 median tissue culture infectious doses per mL (TCID50/mL). For the preparation of serial dilutions of the virus isolates, a minimum essential medium was employed. To assess the specificity of the sensor, swine viral pathogens, such as H1N2, H3N2, porcine circovirus 2d (PCV 2d), and porcine reproductive and respiratory syndrome virus (PRRSV), were utilized. Swine oral fluids, nasal swabs, and lung tissue homogenates were selected from the samples submitted to the Iowa State University Veterinary Diagnostic Laboratory. These samples underwent IAV RT-qPCR testing to confirm their status. In this step, nucleic acids were isolated from 100 μL virus cultures or swine clinical specimens using a commercial RNA/DNA extraction kit (MagMAX Pathogen, Thermo Fisher Scientific, Waltham, MA, USA) and an automated extraction system (Kingfisher Flex, same supplier), following the instructions of the manufacturer. The extracted nucleic acids were collected with 90 μL of elution buffer. For PCR assay, a commercial IAV RT-qPCR kit targeting the matrix and nucleoprotein genes (VetMAX-Gold SIV One-Step RT-PCR kit, Thermo Fisher Scientific, Waltham, MA, USA) were employed.[43] Cyclic threshold (Ct) values from the PCR test were recorded for virus samples diluted at various concentrations that were obtained. Samples showing a Ct value less than 38 were considered IAV positive, while those with Ct values of 38 or higher were classified as negative.

Formation of Hydrophilic, Conducting Sponge. Commercial sugar cubes with a side length of 10 mm and an approximate particle size of 400 μm were utilized as templates for the creation of sponge cubes.[44−47] As shown in Figure 2a, the sugar cubes were arranged within a Petri dish and subsequently submerged in a solution composed of an equal volume ratio of Type A and Type B components of Ecoflex silicone (00-30; Smooth-on, Inc.). The Petri dish was then placed inside a vacuum degasser for 30 min, facilitating the mixture to infiltrate into the sugar cube templates due to the induced pressure difference. The Petri dish was then transferred onto a 60 °C hot plate and left to cure for 3 h. Following the curing process, the sugar templates infused with Ecoflex silicone were extracted from the Petri dish and immersed in deionized (DI) water within an ultrasonic cleaner set at 45 °C for 30 min. They were then given a DI water rinse. The resulting Ecoflex sponge, featuring its interconnected pores between silicone-based scaffolds, was dried in an oven at 60 °C for 30 min. To ensure all pores were expanded, the sponge was immersed in toluene for 2 h, followed by an ethanol rinse to remove excess toluene.

In order to enhance the electrical conductivity of the sponge, it was immersed in a dispersion of graphene flakes at a concentration of 50 mg/mL for 1 h (Figure 2a). This enabled the flakes to spread throughout the pores of the sponge, eventually forming a graphene layer on the scaffold surface after being baked at 90 °C for 12 h. This immersion and baking process was repeated several times to ensure high conductivity. Subsequently, 1 mg/mL dispersion of rGO was drop-cast onto the sponge, making its surface hydrophilic. The final size of the rGO/graphene/sponge composite was reduced by approximately 25% in volume compared to that of the original elastomeric sponge (Figure 2b). Scanning electron microscopy (SEM) images show the modified sponge having a porous feature and being covered by graphene and rGO layers.

Surface Biofunctionalization. The surface of the rGO/graphene/sponge was functionalized with H1N1 antibodies by employing the EDC-NHS chemistry technique. A solution was prepared with EDC (10 mg/mL), sulfo-NHS (10 mg/mL), and antibodies (1 mg/mL), resulting in a final antibody concentration of 15 μg/mL. The sponge was then immersed in this mixture and agitated at a room temperature of 22 °C for 2.5 h. This step facilitated the EDC-NHS cross-linking and the immobilization of antibodies. Following this, the sponge was kept in a humidified chamber at 4 °C for 12 h to stabilize the antibodies. During this process, EDC
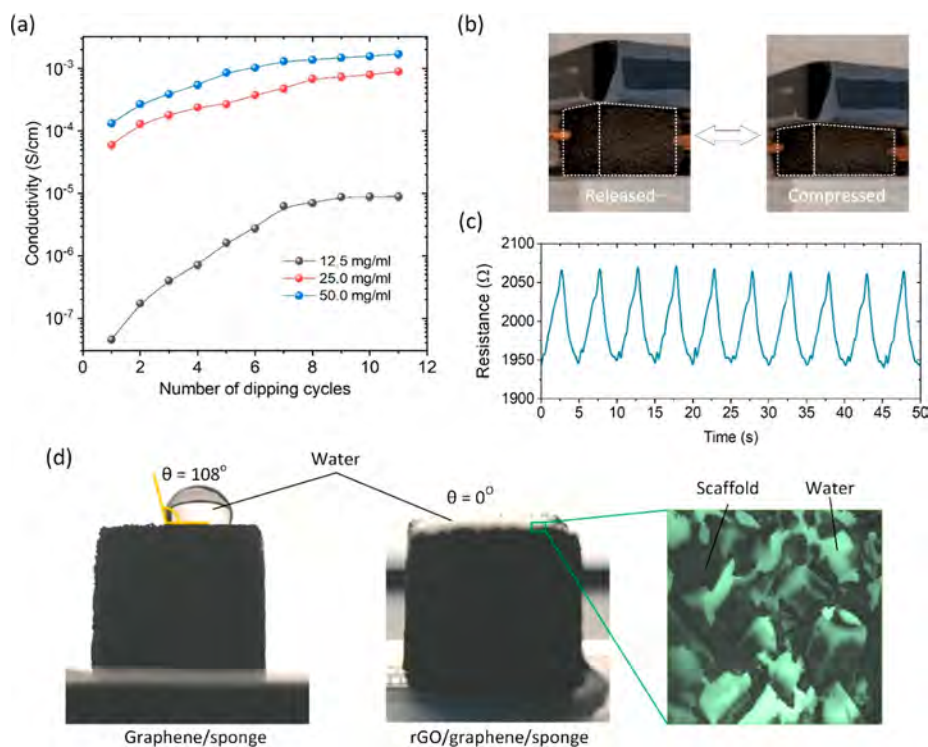
Figure 3. (a) Electrical conductivity of the graphene/sponge as a function of the number of immersion cycles at varying graphene concentrations. (b,c) Optical images (b) and resistance behavior (c) of the graphene/sponge during multiple compression-release cycles. (d) Water contact angle tests for the graphene/sponge (left) and rGO/graphene/sponge (middle), with a fluorescence image (right) highlighting water absorption in the pores of the rGO/graphene/sponge. Here, a dye concentration of 30 μM was prepared by mixing green fluorescein in deionized water. The image was captured using a Leica M205 FCA fluorescence stereo microscope.

interacted with the −COOH groups present on rGO, forming an o-acrylisourea intermediate. This intermediate, in combination with sulfo-NHS, generated a stable NHS ester, which allowed the primary amines of the antibodies to establish covalent C−N bonds.[48] In the final step, the sponge was immersed in a BSA solution (2 mg/mL) to block the nonspecific binding sites on the surface of the sponge.[49]

Sensor Assembly. The housing for both the electrochemical cell and miniature liquid reservoir was formed by 3D printing. The sponge-based WE electrode was fixed to the bottom of the electrochemical cell with an electrically conductive adhesive resin (AA-CARB 61; Atom Adhesives; Fort Lauderdale, FL, USA). The CE was formed by depositing a 5 nm-thick titanium (Ti) and a 100 nm-thick gold (Au) on a polyethylene terephthalate (PET) strip (3 mm × 10 mm × 1 mm) through e-beam evaporation. The RE had the same dimensions as the CE. It was realized by depositing a 300 μm-thick layer of silver/silver chloride (Ag/AgCl; 901773; Sigma-Aldrich; St. Louis MO, USA) paste on another Au/Ti/PET strip via the screen-printing method. All three electrodes were extended to the exterior of the electrochemical cell. The liquid reservoir was used to house a PBS solution and was sealed with Parafilm (HS234526B; Heathrow Scientific; Vernon Hills, IL, USA).

Antibiofouling Considerations. Biofouling on biosensor surfaces presents a challenge that can interfere with the sensor operation. Generally, this issue is caused by several factors, such as nonspecific protein binding at the active sites and microbial growth on the sensor surface. Although our sponge sensor was specifically designed for single use, several strategies were implemented to reduce the potential for biofouling. First, the rGO/graphene/sponge electrode presented a high hydrophilicity. This characteristic is crucial because hydrophilic surfaces are inherently less susceptible to biofouling compared to hydrophobic ones due to the competitive binding of water molecules which reduces the chances of foulant attachment.[50,51] Additionally, BSA was utilized as a blocking agent to create a physical barrier against the nonspecific binding of

proteins[52,53] to the surface of the BSA/antibody/rGO/graphene/sponge electrode.

RESULTS AND DISCUSSION

Physical Characterization. The electrical conductivity of the graphene-infused sponge was observed to rise with an increasing number of cycles of soaking in a dispersion of graphene flakes and baking the sponge, as depicted in Figure 3a. Greater concentrations of graphene flakes could enhance conductivity, provided that the immersion cycles remained the same. However, the growth in conductivity began to slow as the number of cycles continued to rise. This trend was consistent across the three tested dispersion concentrations (12.5, 25, and 50 mg/mL). This could be because the sponge approached its limit for graphene flake uptake, making further immersion cycles less impactful. To achieve optimal conductivity, the sponge was treated with a 50 mg/mL graphene flake concentration and underwent the immersion and baking process eight times.

It is noteworthy that after collecting a liquid sample from a solid surface, the sponge electrode would remain uncompressed during electrochemical measurements. Nevertheless, mechanical stress might be introduced during sweeping across the surface to collect the sample, potentially impacting the conductivity of the sponge. Consequently, it was crucial to revert the sponge to its original resistance when it was transitioned from its compressed to uncompressed state. Figure 3b,c demonstrates consistency in resistance as the sponge returned to its original state following repeated compressions at 25% strain ten times.
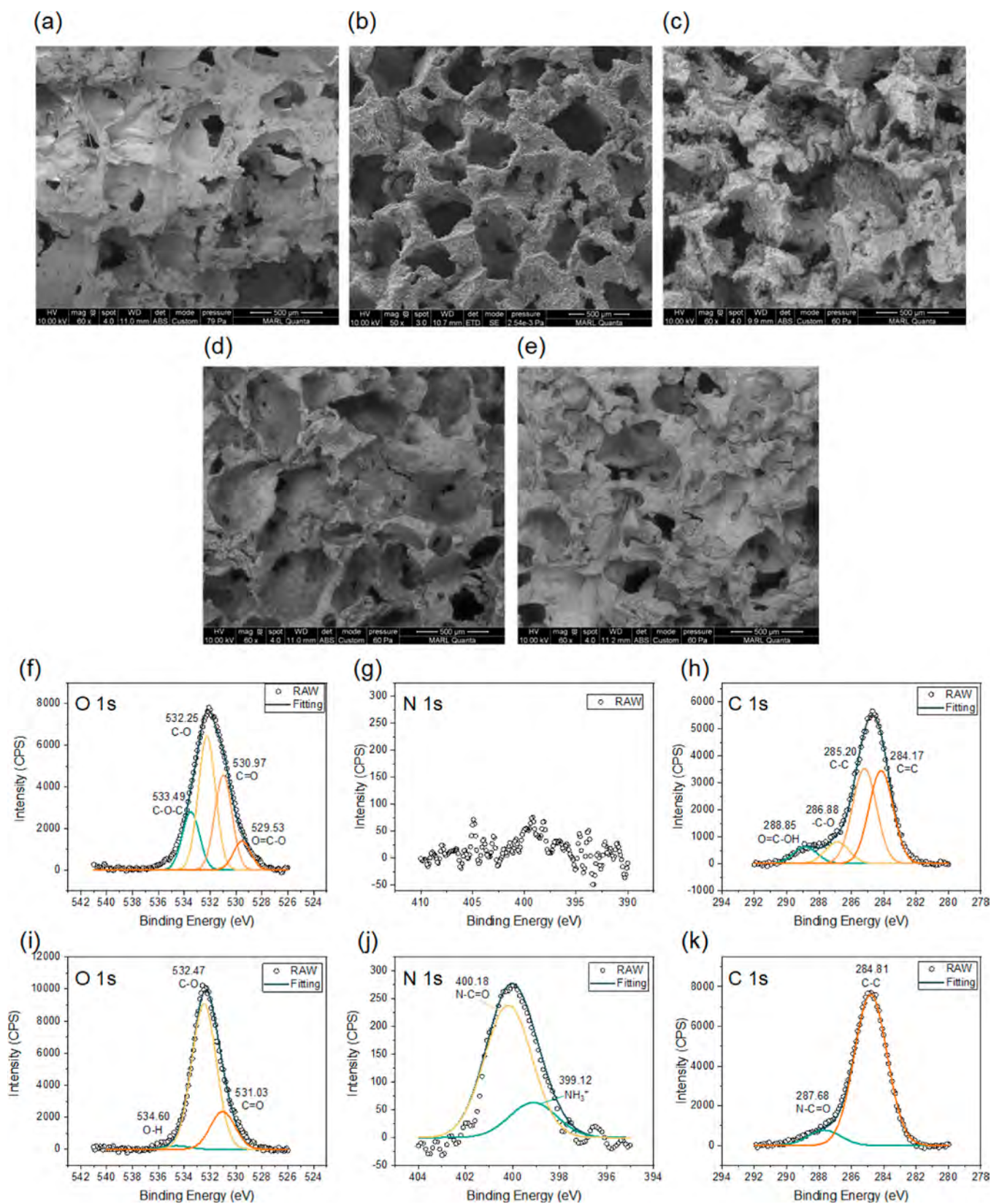
Figure 4. (a−d) SEM images of fabricated Ecoflex sponge (a), graphene/sponge (b), rGO/graphene/sponge (c), and BSA/antibody/rGO/graphene/sponge (d). (e) SEM image of the rGO/graphene/sponge after applying ten cycles of mechanical compression and release. (f−k) XPS analysis for rGO/graphene/sponge and antibody/rGO/graphene/sponge, including the deconvoluted (f), N 1s (g), and C 1s (h) peaks for rGO/graphene/sponge and the deconvoluted (i), N 1s (j), and C 1s (k) peaks for antibody/rGO/graphene/sponge.

Figure 3d demonstrates the alteration of the surface chemistry following the rGO treatment through drop casting.

The treated rGO/graphene/sponge exhibited extremely hydrophilic property, achieving an almost zero-degree water contact
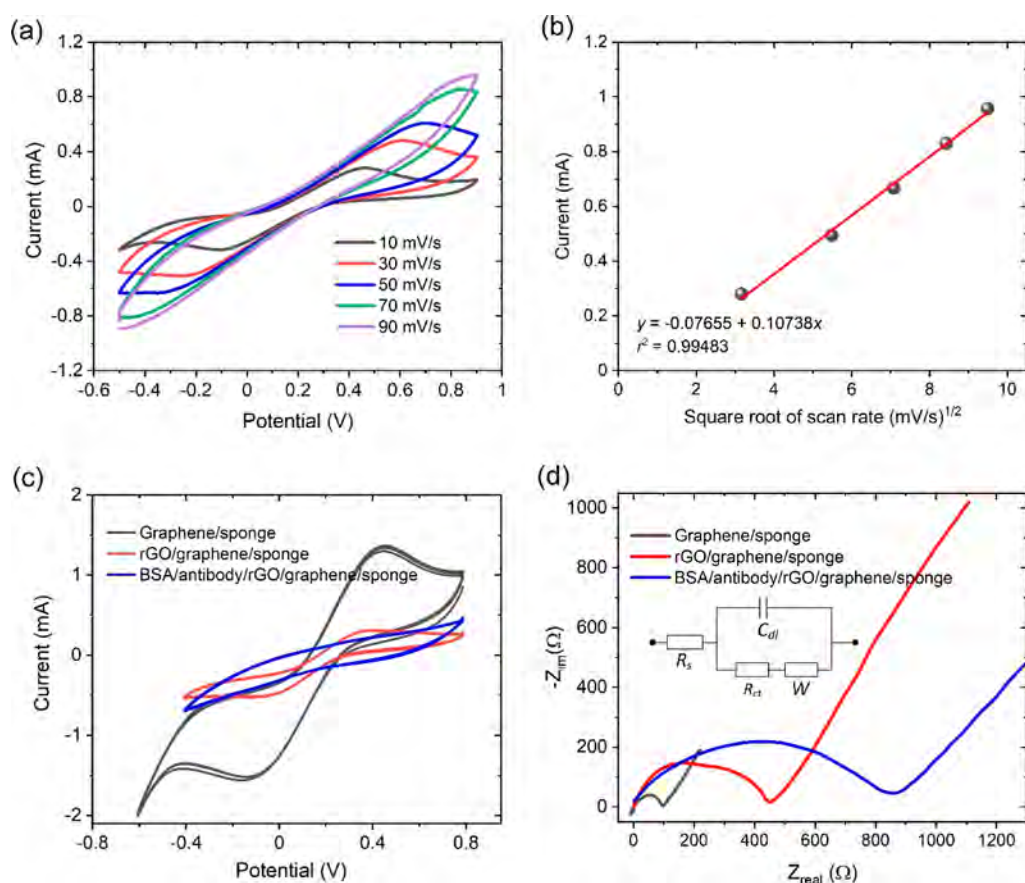
Figure 5. (a) CV results for the rGO/graphene/sponge electrode across varying scan rates. (b) Correlation between anodic peak current and the square root of the scan rate for the rGO/graphene/sponge electrode, with potential relative to the Ag/AgCl reference electrode. (c) CV profiles for the graphene/sponge, rGO/graphene/sponge, and BSA/antibody/rGO/graphene/sponge, each at a consistent scan rate of 10 mV/s. (d) Nyquist plots from the EIS analysis for electrodes referenced in (c), tested between a frequency range of 0.5 Hz to 1 MHz, while maintaining a constant 10 mV potential difference relative to the Ag/AgCl RE. The inset shows the Randles circuit model. For (a−d), the tests were conducted in an electrolyte composed of 5 mM ferro/ferricyanide ($[Fe(CN)_6]^{3−/4}$) and 0.1 M KCl dissolved in PBS at pH = 7.4.

angle. This change can be attributed to the introduction of carboxylic groups on both the inner and exterior scaffold surfaces of the sponge. In contrast, a sponge without the rGO treatment presented a 108-degree water contact angle.

The water absorption capability of the rGO/graphene/ sponge was demonstrated by using water mixed with 30 μM fluorescein. This was verified without any mechanical intervention, such as pressing and releasing the sponge. The instantaneous absorption of liquid within 1 s (Supporting Information Video S1; Supporting Information) implies that capillary forces play a significant role in this process. Figure 3d displays the pores of the sponge fully saturated with water, indicating its effective water absorption properties.

Microscopic Analyses. Scanning electron microscope images (captured using a FEI Quanta-FEG 250 field-emission SEM) revealed details of various materials at different stages in the formation of a virus-specific sponge-based working electrode. These materials included the Ecoflex sponge, graphene/sponge, rGO/graphene/sponge, and BSA/anti-body/rGO/graphene/sponge (Figure 4a−d). The images indicate that the pore sizes of these sponges were a few hundred micrometers and both graphene and rGO were attached to the untreated Ecoflex sponge surface. Additionally, Figure 4e shows the resilience of the rGO/graphene/sponge composite after ten cycles of mechanical compression and release. It underwent ten cycles of compression-release testing,

showing negligible changes in morphology and no apparent cracks. This durability is in line with the resistance dynamics of the rGO/graphene/sponge, as previously demonstrated in Figure 3b,c. Also, energy-dispersive spectroscopy (EDS) analysis, conducted using an Oxford Aztec energy-dispersive spectrometer, on the rGO/graphene/sponge (Figure S1; Supporting Information) reveals clear peaks corresponding to the elements C, O, and Si. Furthermore, traces of Na and Cl were detected, likely originating from residual PBS presented on the material surface.

X-ray Diffraction Analyses. X-ray photoelectron spectroscopy (XPS; Kratos Amicus XPS system) studies were performed on the rGO/graphene/sponge and antibody/rGO/ graphene/sponge. The rGO application was confirmed by a wide scan spectrum in Figure S2a (Supporting Information) that revealed the presence of O 1s (532.3 eV), C 1s (284.5 eV), and Si 2p (103.1 eV). Detailed XPS spectra for the O 1s, N 1s, and C 1s were deconvoluted to their respective binding energies (Figure 4f−k). The deconvoluted O 1s peaks (Figure 4f) appeared at 533.49 eV (C−O−C), 532.25 eV (C−O), 530.97 eV (C=O), and 529.53 eV (O=C−O).[54,55] Similarly, the deconvoluted C 1s peaks (Figure 4h) for the rGO/ graphene/sponge peaks were located at 288.85 eV (O=C− H), 286.88 eV (−C−O), 285.20 eV (C−C), and 284.17 eV (C=C). After the surface biofunctionalization with antibodies, the wide-scan XPS spectrum of the material indicates the
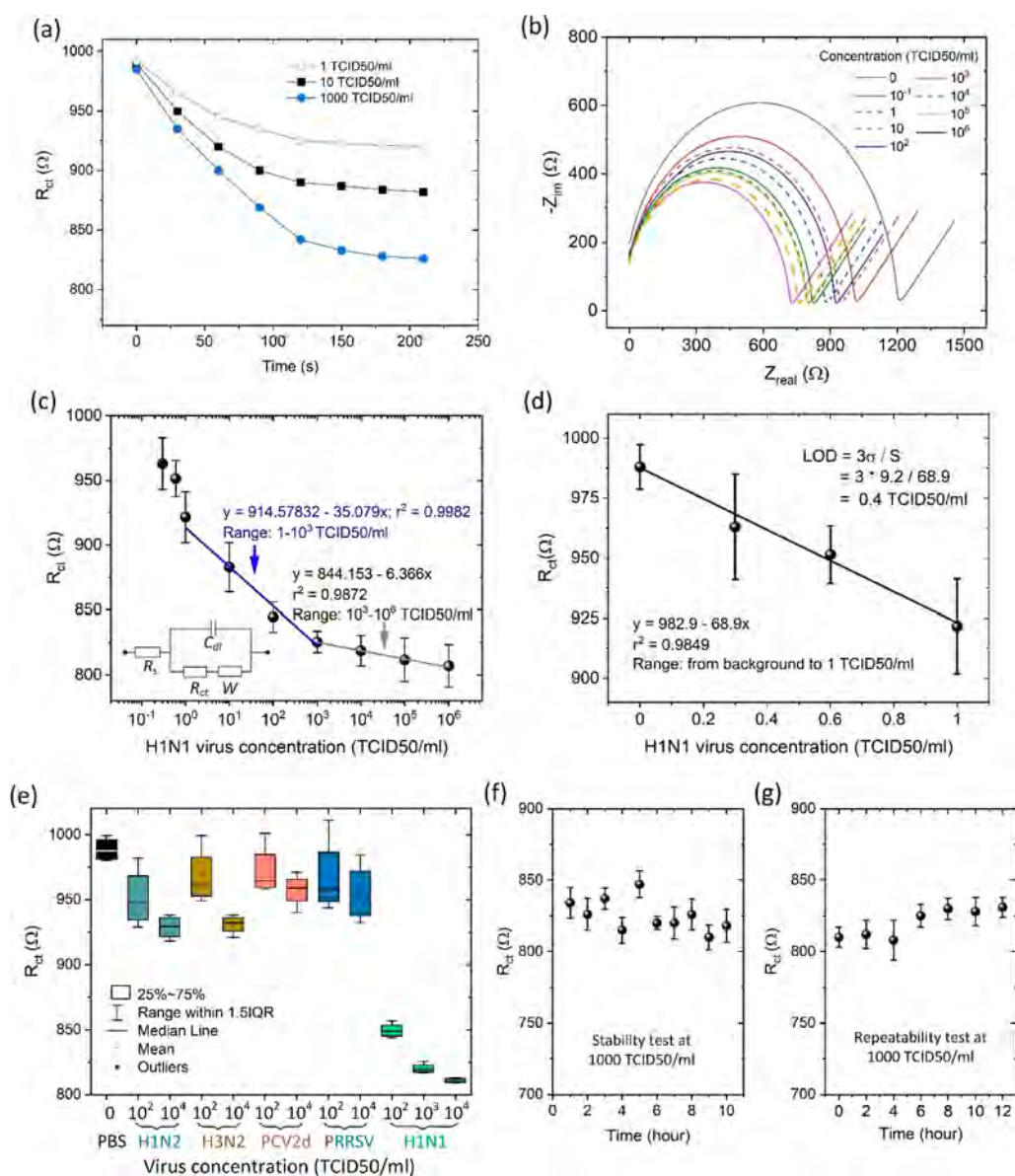
Figure 6. (a) Transient R_{ct} response with the BSA/antibody/rGO/graphene/sponge electrode when exposed to 1, 10, and 1000 TCID50/mL H1N1 in PBS. (b) Nyquist plots across various H1N1 virus concentrations. (c) R_{ct} value of the sensor as a function of H1N1 concentration in the range from 0.5 to 10^6 TCID50/mL, derived from the Nyquist plots in (b) and detailed with the Randles circuit in the inset. (d) R_{ct} value of the sensor as a function of H1N1 concentration in the range from 0 to 1 TCID50/mL. (e) R_{ct} value of the sensor under exposure to PBS and an assortment of swine respiratory viruses, such as H1N2, H3N2, PC 2d, and PRRSV, along with three H1N1 concentrations. Error bars depict the standard deviation from five repeated measurements. (f) R_{ct} value of the sensor under stability test using H1N1 virus at 1000 TCID50/mL. (g) R_{ct} value of the sensor under repeatability test using H1N1 virus at 1000 TCID50/mL.

presence of O, N, C, and Si (Figure S2b; Supporting Information). The O 1s spectrum in Figure 4i suggests the formation of amide bonds (O=C−NH) between the −NH₂ of antibodies and carboxylic groups (O=C−OH) at 529.53 eV. Furthermore, this conversion could be validated in the C 1s spectrum, where the carboxylic peak at 288.85 eV, visible in Figure 4h, was absent in Figure 4k. The amide bond (O=C−NH) at 287.68 eV showed a shift of approximately 1 eV from the carbonyl group (C=O) in the O=C−OH group, possibly due to electron donation from neighboring nitrogen atoms. The presence of P-type orbitals in nitrogen and oxygen atoms facilitates this electron donation, causing a shift in binding energy.[56] This amide group functionalization was further confirmed in the N 1s spectrum at 400.18 eV (Figure 4j).

Electrochemical Characterization. The electrochemical properties of the rGO/graphene/sponge electrode were investigated by using cyclic voltammetry (CV) and electro-chemical impedance spectroscopy (EIS) techniques on a Zive electrochemical workstation (eDAQ, Colorado Spring, CO, USA). The redox electrolyte solution, containing 5 mM ferro/ferricyanide ($[Fe(CN)_6]^{3-/4-}$) and 0.1 M KCl in PBS (pH = 7.4), was utilized for both the CV and EIS studies.

Figure 5a shows that an increase in the scan rate from 10 to 90 mV s⁻¹ led to an increase in the anodic and cathodic peak currents. In Figure 5b, a linear correlation was established between the anodic peak current and the square root of the scan rate, suggesting a diffusion-controlled electrochemical process. This behavior indicates a quasi-reversible redox couple

and free diffusion of redox-active species within the solution.[57] The observed linear relationship aligns with the Randles–Sevcik equation

$$i_p = (2.687 \times 10^5) n^{3/2} A_{el} C^0 (Dv)^{1/2} \tag{1}$$

where i_p is the peak current obtained from cyclic voltametric, n is the number of electrons transferred in the redox event, A_{el} (cm^2) is the electroactive surface area, C^0 (5 mM) is the bulk concentration of the analyte, D (0.16×10^{-6} cm^2 s^{-1}) is the diffusion coefficient of the oxidized analyte, and v (V s^{-1}) is the scan rate.[58] Additionally, Figure 5c compares the cyclic voltammograms stemming from the sponge electrodes with different surface modifications including graphene/sponge, rGO/graphene/sponge, and BSA/antibody/rGO/graphene/sponge. Due to the high conductivity of graphene, the graphene/sponge electrode exhibited an anodic peak current of 1.34 mA. This measurement was about 3.35 times the value observed for the rGO/graphene/sponge electrode (0.40 mA) and 4.96 times that of the BSA/antibody/rGO/graphene/sponge electrode (0.27 mA). The treatment of graphene and rGO led to a lower peak separation potential ΔE of 0.512 V, in comparison to the singular graphene treatment (0.759 V), suggesting a faster charge transfer.[57] The immobilization of antibodies and BSA resulted in the CV curve adopting a quasirectangular shape, indicative of capacitive or battery-like behavior of the electrode.

EIS was employed to probe the interfacial characteristics of sponge electrodes having varied surface modifications in relation to the ferro- and ferricyanide redox reaction. The resulting Nyquist plots were analyzed by the Randles circuit model, incorporating the charge transfer resistance R_{ct}, the double layer capacitance C_{dl}, and the Warburg impedance W (Figure 5d). To obtain the real (Z') and imaginary ($-Z''$) components of the complex impedance at different frequencies for a parallel RC circuit, R_{ct} and C_{dl} values were calculated using eq 2.[58]

$$\begin{aligned} Z(\omega) &= R_s + \frac{R_{ct} + W}{1 + j\omega(R_{ct} + W)C_{dl}^2} \\ &= R_s + \frac{R_{ct} + W}{1 + \omega^2(R_{ct} + W)^2 C_{dl}^2} \\ &\quad - j\frac{\omega(R_{ct} + W)^2 C_{dl}}{1 + \omega^2(R_{ct} + W)^2 C_{dl}^2} \end{aligned} \tag{2}$$

The graphene/sponge electrode exhibited a R_{ct} value of 80.5 Ω. Further modification with rGO increased the R_{ct} value to 355.3 Ω, attributable to the low conductivity of rGO. The immobilization of antibodies and BSA proteins provided an insulative layer, impeding the redox conversion of [Fe(CN)$_6$]$^{3-/4-}$ and pushing the R_{ct} value to 390.8 Ω.

Additionally, to evaluate the electron transfer between the electroactive species and the modified sponge electrodes, the heterogeneous electron transfer rate constants (k_s) were deduced for the varied sponge electrodes. The equation $k_s = RT/(n^2 F^2 A R_{ct} C)$ was applied, wherein R is the gas constant (8.314 J K^{-1} mol^{-1}), T is the temperature (298 K), n is the electron transfer constant of the redox couple, F is Faraday's constant, A is the surface area of the electrode, and C is the concentration of the redox couple within the electrolyte. The derived k_s value for the graphene/sponge electrode (5.10 $\times$ 10^{-6} cm s^{-1}) was higher than that of the rGO/graphene/sponge electrode (1.16 $\times$ 10^{-6} cm s^{-1}). The inclusion of the

insulating antibodies and BSA further impeded the electron transfer, reflecting in the decreased k_s value to 1.05 $\times$ 10^{-6} cm s^{-1} (Table S1; Supporting Information).

Furthermore, the Randles–Sevcik eq (eq 1) was utilized to calculate the electroactive surface area (A_{el}) of the BSA/antibody/rGO/graphene/sponge electrode. At the scan rate of $v = 0.01$ V s^{-1}, the peak current was measured to be 0.27 $\pm$ 0.022 mA (mean $\pm$ standard deviation, from experiments conducted on five identical samples of the BSA/antibody/rGO/graphene/sponge electrodes), leading to an A_{el} of 20.1 $\pm$ 1.77 cm^2. With a corresponding relative standard deviation of 8.8%, the sponge-based sensing electrode demonstrated considerable reproducibility.

Electrochemical Virus Detection. Figure 6 demonstrates the transient response, sensitivity, and selectivity of the sensor to the swine H1N1 virus using the BSA/antibody/rGO/graphene/sponge electrode. The transient response test determined the incubation time required for stable immuno-complex formation between the immobilized antibodies and H1N1 virus. The sensor was first exposed to a 1 TCID50/mL H1N1 concentration of H1N1 virus in PBS (pH = 7.4; containing 5 mM [Fe(CN)$_6$]$^{3-/4}$ and 0.1 M KCl). After each exposure interval, the sensor was rinsed with PBS to remove the unbound virus before the EIS measurement. R_{ct} values, derived from their corresponding Nyquist plots via the Randles circuit, showed a decline over time (Figure 6a), indicating the virus binding to the immobilized antibodies on the sensor surface. Notably, the R_{ct} began to decrease in the first minute and plateaued around the 2 min mark, establishing an incubation time for the sensor. Furthermore, the incubation time appeared to be almost unaffected by varying concentrations of H1N1 virus. This observation was based on the R_{ct} responses of the sensor to three virus concentrations at 1, 10, and 1000 TCID50/mL in PBS at pH = 7.4 containing 5 mM [Fe(CN)$_6$]$^{3-/4}$ and 0.1 M KCl (Figure 6a).

Next, the sensitivity of the sensor was evaluated using various concentrations of the swine H1N1 virus, ranging from 3×10^{-1} to 1×10^6 TCID50/mL. These concentrations were prepared by diluting a stock H1N1 virus in PBS (pH = 7.4; containing 5 mM [Fe(CN)$_6$]$^{3-/4}$ and 0.1 M KCl). The baseline R_{ct} of the sensor was recorded at 982.4 Ω in PBS without the virus. The sensor was exposed to different H1N1 samples for the established 2 min incubation and subsequently cleaned with PBS. The cleaning procedure involved pressing the PBS reservoir against the sharp edges of the electrochemical cell to rupture the sealing film. This was followed by the discharging of the PBS solution from the reservoir. Subsequently, the electrochemical cell with the reservoir still attached was gently shaken to enhance the cleaning process. Finally, the electrochemical cell was inverted and placed on an absorbent tissue paper to allow the PBS solution to be absorbed by the paper (Figure S4). Figure 6b shows the Nyquist plots from different virus concentrations. At 1 TCID50/mL, the R_{ct} value of the sensor reduced to 921.6 Ω and further decreased to 825.5 Ω at 10^3 TCID50/mL. As the concentration rose further beyond 10^3 TCID50/mL, the R_{ct} value continued dropping, but the decline rate significantly slowed down. A log–linear calibration curve was plotted for the sensitivity, showing −35.08 Ω/log(TCID50/mL) for the 1 to 10^3 TCID50/mL range and −6.37 Ω/log(TCID50/mL) from 10^3 to 10^6 TCID50/mL (Figure 6c). Interestingly, the sensor responded linearly to virus concentrations below 1 TCID50/mL with the highest sensitivity at −68.90 Ω/
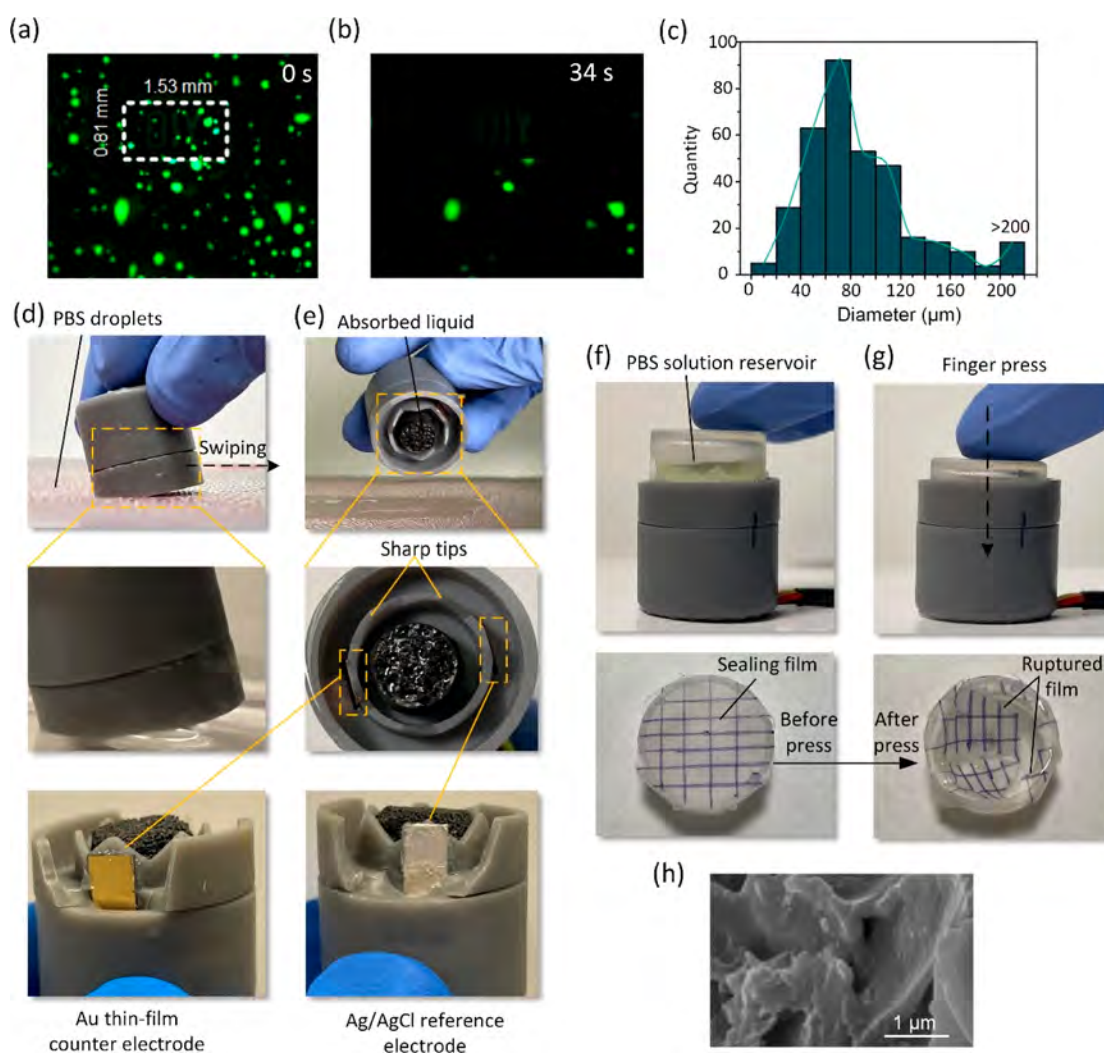
Figure 7. (a,b) Time-lapsed fluorescence images of the droplets sprayed on the tabletop surface using the fine mist spray, at time $t = 0$ (a) and 34 (b). (c) Size distribution for the droplets sprayed on the tabletop surface at time $t = 0$. (d) Collection of liquid from the moistened tabletop surface that was treated with virus samples. (e) Sponge displaying an absorbed liquid sample. Details about the sharp tips, the Au-based CE, and the Ag/AgCl-based RE within the electrochemical cell are given in the inset. To facilitate the visualization of the CE and RE, the outer circular wall of the electrochemical cell was partially broken. (f) Prepressed miniature PBS reservoir adjacent to the sharp edges of the electrochemical cell housing the sponge. (g) Activation of the reservoir by the finger pressure resulted in the release of the PBS solution into the cell for virus incubation and detection. (h) SEM image of the sponge with virus particles. Note that the virus was administrated onto the table at 10 TCID50/mL.

TCID50/mL (Figure 6d). Over the entire concentration range from 3×10^{-1} to 1×10^6 TCID50/mL, the R_{ct} reduced with increasing H1N1 virus concentration (Figure 6c,d). This trend is consistent with findings from several studies, where an increase in current or a reduction in impedance was noted.[59−61] The formation of antibody-virus immunocomplexes impacted the charge transport through the electrical double layer at the electrode−electrolyte interface, increasing the charge count and lowering the R_{ct}. However, contrarily, many other studies have reported the opposite trend, where R_{ct} increases as H1N1 virus concentration increases.[62−64] These different observations could be attributed to a range of complex factors, often linked to changes in the physical and chemical properties of the electrode surface and the electrochemical environment at the electrode−electrolyte interface, especially in the context of immunocomplex formation at a specific electrode surface in a particular environment.

The limit of detection (LOD) for the sensor was determined using its linear response for concentration below 1 TCID50/

mL (Figure 6d) and applying the $3\,\sigma/S$ method, where σ is the standard deviation for the baseline signal and S is the sensitivity of the sensor within the linear range. The LOD was calculated to be approximately 0.4 TCID50/mL (derived from the calculation $3 \times 9.2/68.9$). However, as discussed later, for practical purposes and to ensure accurate detection of the H1N1 virus in the presence of other IAV strains, the effective detection range for H1N1 was set higher than the calculated LOD.

The specificity of the sensor was assessed by exposing it to two other swine IAV subtypes, namely, H1N2 and H3N2, and two additional swine respiratory viral pathogens, PCV 2d and PRRSV. As illustrated in Figure 6e, the R_{ct} value of the sensor showed a modest reduction of −3.8 and −6.3% from its baseline when introduced to H1N2 concentrations of 10^2 and 10^4 TCID50/mL, respectively. In response to H3N2 at the same concentrations as H1N2, the R_{ct} variations were nearly parallel, exhibiting changes of −2.2 and −6.8%. For PCV 2d and PRRSV at a 10^2 TCID50/mL concentration, the R_{ct} value
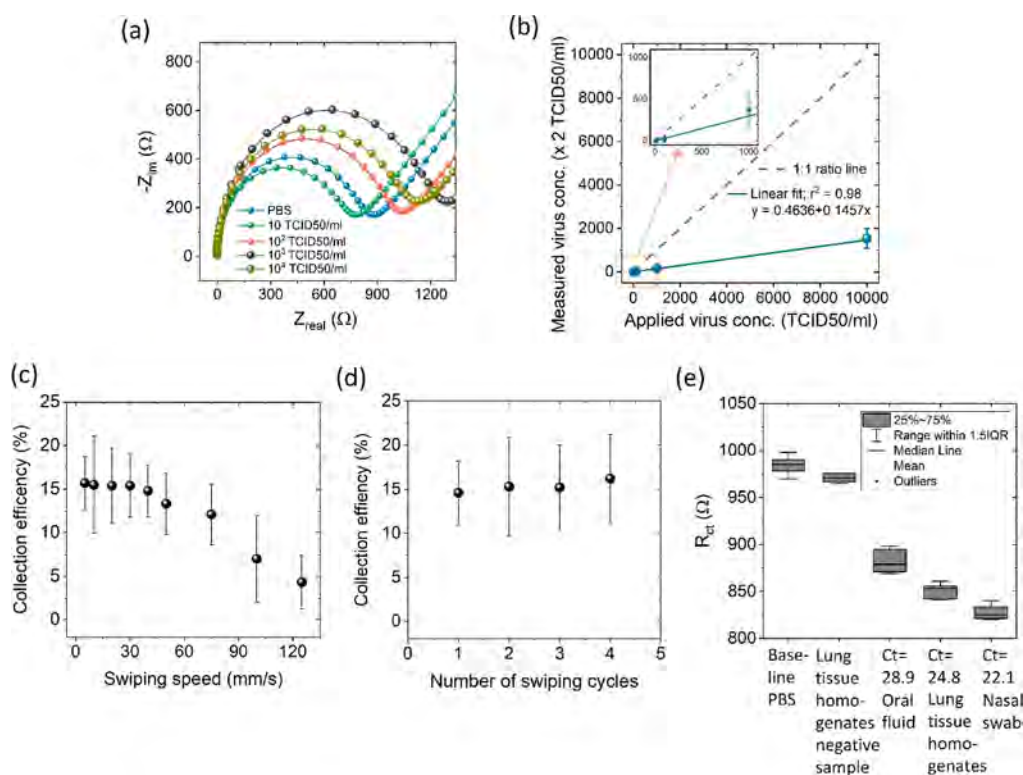
Figure 8. (a) Nyquist plots of the sensor responding to four H1N1 concentrations collected from the table. (b) Correlation between the measured and applied H1N1 concentrations, considering a dilution factor of 2. The inset shows a close-up in the low concentration range. (c,d) Virus collection efficiency versus swiping speed (c) and swiping cycle (d). The applied H1N1 virus concentration was 10 TCID50/mL. The collection efficiency refers to the ratio of the concentration measured to the concentration applied. (e) R_{ct} values for one IAV PCR-negative sample and three IAV PCR-positive samples collected from the table surface. Error bars represent the standard deviation of five tests ($n = 5$).

presented a minor drop of −1.7 and −2.1%. This drop became slightly more pronounced at a 10^4 TCID50/mL concentration, with R_{ct} reductions of −3.1 and −3.4%, respectively. The sensor reacted somewhat more to the IAV subtypes than to the PCV 2d and PRRSV viruses, which could be due to increased nonspecific binding. Notably, following these interference tests, the ability of the sensor to detect H1N1 virus was re-evaluated, using three H1N1 samples at concentrations of 10^2, 10^3, and 10^4 TCID50/mL. The result showed a similar decrease in R_{ct} to what it displayed before exposure to the interfering viruses, indicating that the sensor retained its specific affinity for the H1N1 virus, even when presented with other pathogens.

It is important to note that when the sensor was exposed to nontarget H1N2 and H3N2 virus, there was a decrease in the R_{ct} value by 6.8 and 6.3%, respectively. In comparison, the target H1N1 virus at a concentration of 1 TCID50/mL caused a consideration R_{ct} reduction by 7.3%. This reduction was only marginally higher than that induced by the nontarget viruses (Figure 6e). Consequently, to identify the presence of the H1N1 virus, a reduction in R_{ct} greater than 7.3% should be observed. Given these findings, the practical detection range of the sensor for the H1N1 virus was established between 1 and 10^6 TCID50/mL. This range was chosen despite the calculated LOD being as low as 0.4 TCID50/mL to ensure reliability in detecting H1N1 virus amidst potential interference from other IAV strains.

Stability and Repeatability. The stability of the sensor was assessed by detecting H1N1 virus at a concentration of 1000 TCID50/mL in PBS (pH = 7.4; containing 5 mM $[Fe(CN)_6]^{3-/4-}$ and 0.1 M KCl). This evaluation was performed ten times over an hour with a 1 h interval. Between two consecutive measurements, the sensor was cleaned with a PBS solution, gently dried with tissue paper, and stored in a humid environment at 4 °C. The mean value of R_{ct} was found to be 825.3 Ω with a relative standard deviation of 3.1%, as shown in Figure 6f. To evaluate the repeatability of the sensor, another test was conducted by exposing the sensor to H1N1 virus at 1000 TCID50/mL for a duration of 12 h. Measurements of the R_{ct} value were taken every 2 h without changing the virus sample or intervening the sensor. The result (Figure 6g) indicates a mean value of R_{ct} = 818.2 Ω with a relative standard deviation of 5.5%, indicating considerable repeatability over extended exposure.

Collecting and Detecting Virus Particles on Solid Surfaces. We sought to simulate a scenario where respiratory viruses settle on solid surfaces, droplets carrying the viruses evaporate, and the viruses are exposed to the air, as opposed to remaining within droplets. To achieve this, we designed an experiment that involved preparing a virus-contaminated surface, utilizing our sensor to collect virus samples from the surface and performing electrochemical analysis to determine the H1N1 virus concentration. The first step involved spraying a virus suspension solution on the surface using a fine mist sprayer. After spraying the droplets of the virus suspension solution, we did not immediately use the sponge to collect them. Instead, we allowed the droplets to evaporate naturally, leaving the virus particles on the surface. This approach aimed at closely resembling a contaminated surface, which may not appear to be visibly wet. Finally, we misted the dry, virus-contaminated surface by spraying droplets of PBS without any

virus on the table surface. This step was designed to facilitate the collection of virus samples using a sponge, simulating the process of gathering virus particles from a contaminated surface for electrochemical analysis.

More specifically, the sensor established a baseline R_{ct} of 985.8 Ω in PBS. We then prepared four H1N1 virus concentrations (10, 10^2, 10^3, and 10^4 TCID50/mL) by diluting the stock virus in PBS. Our fine mist sprayer (Fine Mist Atomizer, Hydior) dispersed the H1N1 virus suspension solution onto a chemical-resistant phenolic tabletop to create a virus-contaminated surface. The size distribution of the mist droplets was analyzed by using Matlab (Figure 7a), revealing that most droplets were between 20 and 200 μm in diameter (Figure 7c). This droplet size range is comparable to those produced using other methods used in virus transmission research, such as spray bottles[65] and nebulizers.[66] Also, it should be noted that, in these studies, PBS is often employed to prepare virus samples for droplet generation.[67] In our experiment, approximately 34 s after spraying, most droplets on the tabletop evaporated (Figure 7b). Ten minutes after the spraying, the tabletop was almost completely dry.

To collect viruses from the virus-contaminated surface using the sponge, 2 mL of PBS was sprayed on the table to wet the surface area where the virus sample had been sprayed previously. The thickness of the mist layer is not uniform, ranging from 50−250 μm (Figure S3; Supporting Information). Subsequently, the sponge was gently passed over the misted surface to collect the liquid (Figure 7d,e). The swiping speed was about 30 mm/s. Next, the PBS solution reservoir of the sensor was pressed against the sharp edges of the circular fence, causing the sealing film of the reservoir to rupture (Figure 7f,g). The PBS was released from the reservoir, immersing the entire sponge in the electrochemical cell. About 4 mL of PBS solution was required for full immersion. The sponge was left to rest for 2 min, allowing for incubation (Figure 7h) at the surface of the sponge.

After the incubation, EIS measurements were conducted, producing the responses displayed in Figure 8a. As the concentration of the sprayed virus sample increased, the R_{ct} value of the sensor showed a decrease. The detected virus concentration was deduced from the corresponding R_{ct} value by using the calibration graph in Figure 8c. Given that the collected virus sample was in 4 mL of PBS solution, whereas the initial virus sample was only 2 mL, the deduced virus concentration was multiplied by a factor of 2 to calculate the measured actual virus concentration. Figure 8b demonstrates a correlation between the applied and measured virus concentrations, characterized by a slope of 0.146 and r^2 = 0.98. This slope, indicating the ratio of measured to applied concentration, represented the virus collection efficiency of the sponge. The obtained low efficiency could be attributed to various factors. For instance, virus particles might adhere to the table surface after settling and not be effectively absorbed by the sponge with the PBS solution. Additionally, once the sponge was saturated with the solution, its capacity to attract more solution through the capillary force would be reduced, leaving some virus particles on the surface. Moreover, even if virus particles were initially absorbed into the sponge, they might be flushed out during loading the PBS solution from the integrated reservoir into the sponge due to possible insufficient binding to the interior surface of the sponge. Given these multiple plausible factors, quantifying the impact of each factor would present a significant challenge.

Interestingly, when the swiping speed increased from 30 to 75 mm/s, the virus collection efficiency only marginally decreased from 14.6 to 12%. Slowing the swiping speed below 30 mm/s showed negligible improvement in efficiency, whereas going beyond 100 mm/s led to a notable drop in efficiency, as depicted in Figure 8c. When operating at 30 mm/s, multiple swipes across the same surface area had a minimal impact on improving the collection efficiency (Figure 8d). Nevertheless, this test demonstrated that at a moderate speed using the sponge sensor can effectively collect virus samples from a solid surface, resulting in a considerable correlation with the actual quantity of the target virus.

The proof-of-concept of the device to detect the H1N1 virus was further demonstrated by evaluating one IAV PCR-negative lung tissue homogenate and three IAV PCR-positive samples (Figure 8e). The positive samples included a nasal swab with Ct = 22.1, a lung tissue homogenate with Ct = 24.6, and an oral fluid with Ct = 28.9. Each of these was applied to the tabletop and then gathered by using the sponge sensor following the previously outlined procedure for H1N1 virus samples. The result revealed that for the negative samples, the R_{ct} value was only slightly beneath the baseline, suggesting the minimal presence of H1N1 virus. Meanwhile, the R_{ct} values significantly dropped for the positive samples, pointing to higher concentrations of the H1N1 virus.

■ CONCLUSIONS

We developed a sponge sensor for rapid on-site virus detection on solid surfaces. Utilizing the water-absorbing ability of a conducting porous sponge modified with rGO, graphene, and specific antibodies, this sensor could collect, identify, and quantify virus particles directly from the surfaces. To operate, PBS solution was sprayed to moisten the target area, which was then dried with the sponge. Releasing the electrolyte solution required a simple finger press. After 2 min incubation, the sensor provided the concentration of the target virus. The calculated LOD of the sensor was 0.4 TCID50/mL for H1N1 virus, while the practical detection range covered from 1 to 10^6 TCID50/mL. Compared to other electrochemical H1N1 virus sensors,[68−75] our sensor offered a wide dynamic detection range and a short detection time (Table S2, Supporting Information). A single sponge swipe collected about 15% of the virus particles from the moistened area. In our proof-of-concept demonstration, several swine H1N1 virus-positive samples were used to create virus-contaminated surfaces, accompanied by a negative control sample. Our sponge sensor showed its ability to collect virus samples from the surface and then perform electrochemical analysis to determine the H1N1 virus concentration. The integration of a press-release mechanism enhanced its portability, making it convenient for on-site detection. We envision the possibility of integrating multiple sponge-based sensing elements into a single device, allowing for simultaneous detection of different viruses. Additionally, incorporating affordable electronic readout circuits could transform our sponge sensor into a compact, rapid, and multipurpose detection tool suitable for on-site surveillance of multiple viruses. Given the context of the COVID-19 pandemic, this device holds great potential for adaptation in the detection of the SARS-CoV-2 virus. By substituting the recognition molecules for the H1N1 IAV with those specific to the SARS-CoV-2 virus during surface functionalization, our sensor could detect this virus. Last, it is worth noting that there remains considerable room to

improve biofouling mitigation. Future strategies might include the integration of antifouling agents[76] and the application of electrostatic repulsion techniques[77] to repel charged biomolecules for minimizing nonspecific adsorption.

ASSOCIATED CONTENT

Supporting Information

The Supporting Information is available free of charge at https://pubs.acs.org/doi/10.1021/acssensors.3c02766.

Calculated values of charge transfer resistance (R_{ct}), double-layer capacitance (C_{dl}), Warburg impedance (W), and heterogeneous electron transfer rate constant (k_s) of various sponge-based electrodes used in the electrochemical virus sensor; comparison of the presented virus sensor with other portable sensors for detecting H1N1 virus; EDS spectrum of the fabricated antibody/rGO/graphene/sponge sample; wide-scan spectra of the rGO/graphene/sponge and antibody/rGO/graphene/sponge samples; side view of the mist layer formed on a table surface following the spraying droplets of 2 mL of PBS using a fine mist sprayer; and key cleaning steps for the sponge electrode within the electrochemical cell (PDF)

Instantaneous absorption of liquid within 1 s using the fabricated sponge (MP4)

AUTHOR INFORMATION

Corresponding Author

Liang Dong − Department of Electrical and Computer Engineering, Iowa State University, Ames, Iowa 50011, United States; Microelectronics Research Center, Iowa State University, Ames, Iowa 50011, United States; orcid.org/0000-0002-0967-4955; Phone: +1 (515) 294-0388; Email: ldong@iastate.edu

Author

Yang Tian − Department of Electrical and Computer Engineering, Iowa State University, Ames, Iowa 50011, United States

Complete contact information is available at:
https://pubs.acs.org/10.1021/acssensors.3c02766

Author Contributions

Y.T. designed and fabricated the device and conducted all measurements. L.D. conceived the sensor concept and supervised the research of Y.T. Both authors analyzed data. Y.T. drafted the manuscript. L.D. provided inputs to the draft.

Notes

The authors declare no competing financial interest.

ACKNOWLEDGMENTS

REFERENCES

(1) Zimmerman, J. J.; Dee, S. A.; Holtkamp, D. J.; Murtaugh, M. P.; Stadejek, T.; Stevenson, G. W.; Torremorell, M.; Yang, H.; Zhang, J. Porcine Reproductive and Respiratory Syndrome Viruses (Porcine Arteriviruses). In Diseases of Swine; John Wiley & Sons, Ltd, 2019; pp 685−708..

(2) Yoon, S.-W.; Webby, R. J.; Webster, R. G. Evolution and Ecology of Influenza A Viruses. In Influenza Pathogenesis and Control - Vol. I; Compans, R. W., Oldstone, M. B. A., Eds.; Current Topics in Microbiology and Immunology; Springer International Publishing: Cham, 2014; pp 359−375..

(3) Wang, C. C.; Prather, K. A.; Sznitman, J.; Jimenez, J. L.; Lakdawala, S. S.; Tufekci, Z.; Marr, L. C. Airborne Transmission of Respiratory Viruses. Science 2021, 373 (6558), No. eabd9149.

(4) Tang, J. W.; Noakes, C. J.; Nielsen, P. V.; Eames, I.; Nicolle, A.; Li, Y.; Settles, G. S. Observing and Quantifying Airflows in the Infection Control of Aerosol- and Airborne-Transmitted Diseases: An Overview of Approaches. J. Hosp. Infect. 2011, 77 (3), 213−222.

(5) Rodríguez-Lázaro, D.; Cook, N.; Ruggeri, F. M.; Sellwood, J.; Nasser, A.; Nascimento, M. S. J.; D'Agostino, M.; Santos, R.; Saiz, J. C.; Rzeżutka, A.; Bosch, A.; Gironés, R.; Carducci, A.; Muscillo, M.; Kovač, K.; Diez-Valcarce, M.; Vantarakis, A.; von Bonsdorff, C.-H.; de Roda Husman, A. M.; Hernández, M.; van der Poel, W. H. M. Virus Hazards from Food, Water and Other Contaminated Environments. FEMS Microbiol. Rev. 2012, 36 (4), 786−814.

(6) Panning, M.; Eickmann, M.; Landt, O.; Monazahian, M.; Ölschläger, S.; Baumgarte, S.; Reischl, U.; Wenzel, J. J.; Niller, H. H.; Günther, S.; Hollmann, B.; Huzly, D.; Drexler, J. F.; Helmer, A.; Becker, S.; Matz, B.; Eis-Hübinger, A. M.; Drosten, C. Detection of Influenza A(H1N1)v Virus by Real-Time RT-PCR. Eurosurveillance 2009, 14 (36), 19329.

(7) Lu, C.-Y.; Chang, L.-Y.; Chen, P.-J.; Xia, N.-S.; Shao, P.-L.; Huang, L.-M. A Highly Specific ELISA for Diagnosis of 2009 Influenza A (H1N1) Virus Infections. J. Formosan Med. Assoc. 2012, 111 (12), 693−697.

(8) Zhang, Y.; Han, H.; Qiu, H.; Lin, H.; Yu, L.; Zhu, W.; Qi, J.; Yang, R.; Pang, Y.; Wang, X.; Lu, G.; Yang, Y. Antiviral Activity of a Synthesized Shikonin Ester against Influenza A (H1N1) Virus and Insights into Its Mechanism. Biomed. Pharmacother. 2017, 93, 636−645.

(9) Chauhan, N.; Narang, J.; Pundir, S.; Singh, S.; Pundir, C. S. Laboratory Diagnosis of Swine Flu: A Review. Artif. Cells, Nanomed., Biotechnol. 2013, 41 (3), 189−195.

(10) Ravina; Dalal, A.; Mohan, H.; Prasad, M.; Pundir, C. S. Detection Methods for Influenza A H1N1 Virus with Special Reference to Biosensors: A Review. Biosci. Rep. 2020, 40 (2), BSR20193852.

(11) Kabay, G.; DeCastro, J.; Altay, A.; Smith, K.; Lu, H.-W.; Capossela, A. M.; Moarefian, M.; Aran, K.; Dincer, C. Emerging Biosensing Technologies for the Diagnostics of Viral Infectious Diseases. Adv. Mater. 2022, 34 (30), 2201085.

(12) Maddali, H.; Miles, C. E.; Kohn, J.; O'Carroll, D. M. Optical Biosensors for Virus Detection: Prospects for SARS-CoV-2/COVID-19. ChemBioChem 2021, 22 (7), 1176−1189.

(13) Goud, K. Y.; Reddy, K. K.; Khorshed, A.; Kumar, V. S.; Mishra, R. K.; Oraby, M.; Ibrahim, A. H.; Kim, H.; Gobi, K. V. Electrochemical Diagnostics of Infectious Viral Diseases: Trends and Challenges. Biosens. Bioelectron. 2021, 180, 113112.

(14) Jin, C. E.; Lee, T. Y.; Koo, B.; Sung, H.; Kim, S.-H.; Shin, Y. Rapid Virus Diagnostic System Using Bio-Optical Sensor and Microfluidic Sample Processing. Sens. Actuators, B 2018, 255, 2399−2406.

(15) Khan, M. S.; Tariq, M. O.; Nawaz, M.; Ahmed, J. MEMS Sensors for Diagnostics and Treatment in the Fight Against COVID-19 and Other Pandemics. IEEE Access 2021, 9, 61123−61149.

(16) Su, D.; Wu, K.; Krishna, V. D.; Klein, T.; Liu, J.; Feng, Y.; Perez, A. M.; Cheeran, M. C.-J.; Wang, J.-P. Detection of Influenza a Virus in Swine Nasal Swab Samples With a Wash-Free Magnetic Bioassay and a Handheld Giant Magnetoresistance Sensing System. Front. Microbiol. 2019, 10, 1077.

(17) Khan, R. R.; Ibrahim, H.; Rawal, G.; Zhang, J.; Lu, M.; Dong, L. Multichannel Microfluidic Virus Sensor for Rapid Detection of

Respiratory Viruses Using Virus-Imprinted Polymer for Digital Livestock Farming. *Sens. Actuators, B* **2023**, *389*, 133920.

(18) Adkins, J. A.; Noviana, E.; Henry, C. S. Development of a Quasi-Steady Flow Electrochemical Paper-Based Analytical Device. *Anal. Chem.* **2016**, *88* (21), 10639−10647.

(19) Benjamin, S. R.; de Lima, F.; Nascimento, V. A. d.; de Andrade, G. M.; Oriá, R. Advancement in Paper-Based Electrochemical Biosensing and Emerging Diagnostic Methods. *Biosensors* **2023**, *13* (7), 689.

(20) Ataide, V. N.; Pradela-Filho, L. A.; Ameku, W. A.; Negahdary, M.; Oliveira, T. G.; Santos, B. G.; Paixão, T. R. L. C.; Angnes, L. Paper-Based Electrochemical Biosensors for the Diagnosis of Viral Diseases. *Microchim. Acta* **2023**, *190* (7), 276.

(21) Lee, D.; Bhardwaj, J.; Jang, J. Paper-Based Electrochemical Immunosensor for Label-Free Detection of Multiple Avian Influenza Virus Antigens Using Flexible Screen-Printed Carbon Nanotube-Polydimethylsiloxane Electrodes. *Sci. Rep.* **2022**, *12* (1), 2311.

(22) Yoo, H.; Shin, J.; Sim, J.; Cho, H.; Hong, S. Reusable Surface Plasmon Resonance Biosensor Chip for the Detection of H1N1 Influenza Virus. *Biosens. Bioelectron.* **2020**, *168*, 112561.

(23) Anusha, J. R.; Kim, B. C.; Yu, K.-H.; Raj, C. J. Electrochemical Biosensing of Mosquito-Borne Viral Disease, Dengue: A Review. *Biosens. Bioelectron.* **2019**, *142*, 111511.

(24) Orooji, Y.; Sohrabi, H.; Hemmat, N.; Oroojalian, F.; Baradaran, B.; Mokhtarzadeh, A.; Mohaghegh, M.; Karimi-Maleh, H. An Overview on SARS-CoV-2 (COVID-19) and Other Human Coronaviruses and Their Detection Capability via Amplification Assay, Chemical Sensing, Biosensing, Immunosensing, and Clinical Assays. *Nano-Micro Lett.* **2021**, *13* (1), 18.

(25) Alam, M. A.; Hasan, M. R.; Anzar, N.; Suleman, S.; Narang, J. Diagnostic Approaches for the Rapid Detection of Zika Virus-A Review. *Process Biochem.* **2021**, *101*, 156−168.

(26) Kumar, N.; Shetti, N. P.; Jagannath, S.; Aminabhavi, T. M. Electrochemical Sensors for the Detection of SARS-CoV-2 Virus. *Chem. Eng. J.* **2022**, *430*, 132966.

(27) Shen, F.; Wang, J.; Xu, Z.; Wu, Y.; Chen, Q.; Li, X.; Jie, X.; Li, L.; Yao, M.; Guo, X.; Zhu, T. Rapid Flu Diagnosis Using Silicon Nanowire Sensor. *Nano Lett.* **2012**, *12* (7), 3722−3730.

(28) Jiang, Z.; Feng, B.; Xu, J.; Qing, T.; Zhang, P.; Qing, Z. Graphene Biosensors for Bacterial and Viral Pathogens. *Biosens. Bioelectron.* **2020**, *166*, 112471.

(29) Meskher, H.; Mustansar, H. C.; Thakur, A. K.; Sathyamurthy, R.; Lynch, I.; Singh, P.; Han, T. K.; Saidur, R. Recent Trends in Carbon Nanotube (CNT)-Based Biosensors for the Fast and Sensitive Detection of Human Viruses: A Critical Review. *Nanoscale Adv.* **2023**, *5* (4), 992−1010.

(30) Manivannan, S.; Ponnuchamy, K. Quantum Dots as a Promising Agent to Combat COVID-19. *Appl. Organomet. Chem.* **2020**, *34* (10), No. e5887.

(31) Nguyen, T. N.; Phung, V.-D.; Tran, V. V. Recent Advances in Conjugated Polymer-Based Biosensors for Virus Detection. *Biosensors* **2023**, *13* (6), 586.

(32) Borges, J. T.; Nakada, L. Y. K.; Maniero, M. G.; Guimarães, J. R. SARS-CoV-2: A Systematic Review of Indoor Air Sampling for Virus Detection. *Environ. Sci. Pollut. Res.* **2021**, *28* (30), 40460−40473.

(33) Pan, M.; Lednicky, J. A.; Wu, C.-Y. Collection, Particle Sizing and Detection of Airborne Viruses. *J. Appl. Microbiol.* **2019**, *127* (6), 1596−1611.

(34) Kim, H. R.; An, S.; Hwang, J. High Air Flow-Rate Electrostatic Sampler for the Rapid Monitoring of Airborne Coronavirus and Influenza Viruses. *J. Hazard. Mater.* **2021**, *412*, 125219.

(35) Blachere, F. M.; Lindsley, W. G.; Slaven, J. E.; Green, B. J.; Anderson, S. E.; Chen, B. T.; Beezhold, D. H. Bioaerosol Sampling for the Detection of Aerosolized Influenza Virus. *Influenza Other Respir. Viruses* **2007**, *1* (3), 113−120.

(36) Raynor, P. C.; Adesina, A.; Aboubakr, H. A.; Yang, M.; Torremorell, M.; Goyal, S. M. Comparison of Samplers Collecting Airborne Influenza Viruses: 1. Primarily Impingers and Cyclones. *PLoS One* **2021**, *16* (1), No. e0244977.

(37) Bofill-Mas, S.; Rusiñol, M. Recent Trends on Methods for the Concentration of Viruses from Water Samples. *Curr. Opin. Environ. Sci. Health* **2020**, *16*, 7−13.

(38) Solo-Gabriele, H. M.; Kumar, S.; Abelson, S.; Penso, J.; Contreras, J.; Babler, K. M.; Sharkey, M. E.; Mantero, A. M. A.; Lamar, W. E.; Tallon, J. J.; Kobetz, E.; Solle, N. S.; Shukla, B. S.; Kenney, R. J.; Mason, C. E.; Schürer, S. C.; Vidovic, D.; Williams, S. L.; Grills, G. S.; Jayaweera, D. T.; Mirsaeidi, M.; Kumar, N. Predicting COVID-19 Cases Using SARS-CoV-2 RNA in Air, Surface Swab and Wastewater Samples. *Sci. Total Environ.* **2023**, *857*, 159188.

(39) Gibson, K. E.; Crandall, P. G.; Ricke, S. C. Removal and Transfer of Viruses on Food Contact Surfaces by Cleaning Cloths. *Appl. Environ. Microbiol.* **2012**, *78* (9), 3037−3044.

(40) Mihucz, V. G.; Ruus, A.; Raamets, J.; Wimmerová, L.; Vera, T.; Bossi, R.; Huttunen, K. A Review of Microbial and Chemical Assessment of Indoor Surfaces. *Appl. Spectrosc. Rev.* **2022**, *57* (9−10), 817−889.

(41) Ali, M. A.; Singh, C.; Srivastava, S.; Admane, P.; Agrawal, V. V.; Sumana, G.; John, R.; Panda, A.; Dong, L.; Malhotra, B. D. Graphene Oxide-Metal Nanocomposites for Cancer Biomarker Detection. *RSC Adv.* **2017**, *7* (57), 35982−35991.

(42) Zhang, J.; Gauger, P. C. Isolation of Swine Influenza A Virus in Cell Cultures and Embryonated Chicken Eggs. *Methods Mol. Biol.* **2020**, *2123*, 281−294.

(43) Zhang, J.; Harmon, K. M. RNA Extraction from Swine Samples and Detection of Influenza A Virus in Swine by Real-Time RT-PCR. *Methods Mol. Biol.* **2020**, *2123*, 295−310.

(44) Ding, Y.; Xu, T.; Onyilagha, O.; Fong, H.; Zhu, Z. Recent Advances in Flexible and Wearable Pressure Sensors Based on Piezoresistive 3D Monolithic Conductive Sponges. *ACS Appl. Mater. Interfaces* **2019**, *11* (7), 6685−6704.

(45) Zhu, D.; Handschuh-Wang, S.; Zhou, X. Recent Progress in Fabrication and Application of Polydimethylsiloxane Sponges. *J. Mater. Chem. A* **2017**, *5* (32), 16467−16497.

(46) Ke, K.; McMaster, M.; Christopherson, W.; Singer, K. D.; Manas-Zloczower, I. Highly Sensitive Capacitive Pressure Sensors Based on Elastomer Composites with Carbon Filler Hybrids. *Composites, Part A* **2019**, *126*, 105614.

(47) Yao, H.-B.; Ge, J.; Wang, C.-F.; Wang, X.; Hu, W.; Zheng, Z.-J.; Ni, Y.; Yu, S.-H. A Flexible and Highly Pressure-Sensitive Graphene-Polyurethane Sponge Based on Fractured Microstructure Design. *Adv. Mater.* **2013**, *25* (46), 6692−6698.

(48) Ali, M. A.; Hong, W.; Oren, S.; Wang, Q.; Wang, Y.; Jiang, H.; Dong, L. Tunable Bioelectrodes with Wrinkled-Ridged Graphene Oxide Surfaces for Electrochemical Nitrate Sensors. *RSC Adv.* **2016**, *6* (71), 67184−67195.

(49) Zhang, Q.; Loghry, H. J.; Qian, J.; Kimber, M. J.; Dong, L.; Lu, M. Towards Nanovesicle-Based Disease Diagnostics: A Rapid Single-Step Exosome Assay within One Hour through in Situ Immuno-magnetic Extraction and Nanophotonic Label-Free Detection. *Lab Chip* **2021**, *21* (18), 3541−3549.

(50) Lin, P.-H.; Li, B.-R. Antifouling Strategies in Advanced Electrochemical Sensors and Biosensors. *Analyst* **2020**, *145* (4), 1110−1120.

(51) Hanssen, B. L.; Siraj, S.; Wong, D. K. Y. Recent Strategies to Minimise Fouling in Electrochemical Detection Systems. *Rev. Anal. Chem.* **2016**, *35* (1), 1−28.

(52) Ma, G. J.; Ferhan, A. R.; Jackman, J. A.; Cho, N.-J. Conformational Flexibility of Fatty Acid-Free Bovine Serum Albumin Proteins Enables Superior Antifouling Coatings. *Commun. Mater.* **2020**, *1* (1), 45.

(53) Hu, X.; Tian, J.; Li, C.; Su, H.; Qin, R.; Wang, Y.; Cao, X.; Yang, P. Amyloid-Like Protein Aggregates: A New Class of Bioinspired Materials Merging an Interfacial Anchor with Antifouling. *Adv. Mater.* **2020**, *32* (23), 2000128.

(54) Moreira, V. R.; Lebron, Y. A. R.; da Silva, M. M.; de Souza Santos, L. V.; Jacob, R. S.; de Vasconcelos, C. K. B.; Viana, M. M.

Graphene Oxide in the Remediation of Norfloxacin from Aqueous Matrix: Simultaneous Adsorption and Degradation Process. *Environ. Sci. Pollut. Res.* **2020**, *27* (27), 34513−34528.

(55) Al-Gaashani, R.; Najjar, A.; Zakaria, Y.; Mansour, S.; Atieh, M. A. XPS and Structural Studies of High Quality Graphene Oxide and Reduced Graphene Oxide Prepared by Different Chemical Oxidation Methods. *Ceram. Int.* **2019**, *45* (11), 14439−14448.

(56) Singh, N.; Ali, M. A.; Rai, P.; Ghori, I.; Sharma, A.; Malhotra, B. D.; John, R. Dual-Modality Microfluidic Biosensor Based on Nanoengineered Mesoporous Graphene Hydrogels. *Lab Chip* **2020**, *20* (4), 760−777.

(57) Ali, M. A.; Mondal, K.; Wang, Y.; Jiang, H.; Mahal, N. K.; Castellano, M. J.; Sharma, A.; Dong, L. In Situ Integration of Graphene Foam-Titanium Nitride Based Bio-Scaffolds and Microfluidic Structures for Soil Nutrient Sensors. *Lab Chip* **2017**, *17* (2), 274−285.

(58) Ali, M. A.; Jiang, H.; Mahal, N. K.; Weber, R. J.; Kumar, R.; Castellano, M. J.; Dong, L. Microfluidic Impedimetric Sensor for Soil Nitrate Detection Using Graphene Oxide and Conductive Nanofibers Enabled Sensing Interface. *Sens. Actuators, B* **2017**, *239*, 1289−1299.

(59) Singh, R.; Hong, S.; Jang, J. Label-Free Detection of Influenza Viruses Using a Reduced Graphene Oxide-Based Electrochemical Immunosensor Integrated with a Microfluidic Platform. *Sci. Rep.* **2017**, *7* (1), 42771.

(60) Gattani, A.; Singh, S. V.; Kirthika, P.; Agrawal, A.; Mahawar, M.; Bag, S.; Rajak, K. K.; Singh, R. K.; Singh, P. Fetuin Derivatised Surface for Evaluation of Neuraminidase Inhibitors of Peste Des Petits Ruminants Virus on Electrochemical Impedance Sensor. *Sens. Actuators Rep.* **2021**, *3*, 100047.

(61) Bhardwaj, J.; Sharma, A.; Jang, J. Vertical Flow-Based Paper Immunosensor for Rapid Electrochemical and Colorimetric Detection of Influenza Virus Using a Different Pore Size Sample Pad. *Biosens. Bioelectron.* **2019**, *126*, 36−43.

(62) Dong, S.; Zhao, R.; Zhu, J.; Lu, X.; Li, Y.; Qiu, S.; Jia, L.; Jiao, X.; Song, S.; Fan, C.; Hao, R.; Song, H. Electrochemical DNA Biosensor Based on a Tetrahedral Nanostructure Probe for the Detection of Avian Influenza A (H7N9) Virus. *ACS Appl. Mater. Interfaces* **2015**, *7* (16), 8834−8842.

(63) Fu, Y.; Callaway, Z.; Lum, J.; Wang, R.; Lin, J.; Li, Y. Exploiting Enzyme Catalysis in Ultra-Low Ion Strength Media for Impedance Biosensing of Avian Influenza Virus Using a Bare Interdigitated Electrode. *Anal. Chem.* **2014**, *86* (4), 1965−1971.

(64) Mahshid, S. S.; Flynn, S. E.; Mahshid, S. The Potential Application of Electrochemical Biosensors in the COVID-19 Pandemic: A Perspective on the Rapid Diagnostics of SARS-CoV-2. *Biosens. Bioelectron.* **2021**, *176*, 112905.

(65) Machado, G. T.; Pinto, C. R. d. C.; da Fonseca, L. A. V.; Ramos, T. C. d. S.; Paggi, T. F. P.; Spira, B. Bacteriophages as Surrogates for the Study of Viral Dispersion in Open Air. *Arch. Microbiol.* **2021**, *203* (7), 4041−4049.

(66) Humphrey, B.; Tezak, M.; Lobitz, M.; Hendricks, A.; Sanchez, A.; Zenker, J.; Storch, S.; Davis, R. D.; Ricken, B.; Cahill, J. Viral Preservation with Protein-Supplemented Nebulizing Media in Aerosols. *Appl. Environ. Microbiol.* **2023**, *89* (3), No. e01545−22.

(67) Li, J.; Leavey, A.; Wang, Y.; O'Neil, C.; Wallace, M. A.; Burnham, C.-A. D.; Boon, A. C.; Babcock, H.; Biswas, P. Comparing the Performance of 3 Bioaerosol Samplers for Influenza Virus. *J. Aerosol Sci.* **2018**, *115*, 133−145.

(68) Park, G.; Kim, H.-O.; Lim, J.-W.; Park, C.; Yeom, M.; Song, D.; Haam, S. Rapid Detection of Influenza A (H1N1) Virus by Conductive Polymer-Based Nanoparticle via Optical Response to Virus-Specific Binding. *Nano Res.* **2022**, *15* (3), 2254−2262.

(69) Li, J.; Lin, R.; Yang, Y.; Zhao, R.; Song, S.; Zhou, Y.; Shi, J.; Wang, L.; Song, H.; Hao, R. Multichannel Immunosensor Platform for the Rapid Detection of SARS-CoV-2 and Influenza A(H1N1) Virus. *ACS Appl. Mater. Interfaces* **2021**, *13* (19), 22262−22270.

(70) Lee, D.; Chander, Y.; Goyal, S. M.; Cui, T. Carbon Nanotube Electric Immunoassay for the Detection of Swine Influenza Virus H1N1. *Biosens. Bioelectron.* **2011**, *26* (8), 3482−3487.

(71) Wu, K.; Klein, T.; Krishna, V. D.; Su, D.; Perez, A. M.; Wang, J.-P. Portable GMR Handheld Platform for the Detection of Influenza A Virus. *ACS Sens.* **2017**, *2* (11), 1594−1601.

(72) Han, J.-H.; Lee, D.; Chew, C. H. C.; Kim, T.; Pak, J. J. A Multi-Virus Detectable Microfluidic Electrochemical Immunosensor for Simultaneous Detection of H1N1, H5N1, and H7N9 Virus Using ZnO Nanorods for Sensitivity Enhancement. *Sens. Actuators, B* **2016**, *228*, 36−42.

(73) Bai, C.; Lu, Z.; Jiang, H.; Yang, Z.; Liu, X.; Ding, H.; Li, H.; Dong, J.; Huang, A.; Fang, T.; Jiang, Y.; Zhu, L.; Lou, X.; Li, S.; Shao, N. Aptamer Selection and Application in Multivalent Binding-Based Electrical Impedance Detection of Inactivated H1N1 Virus. *Biosens. Bioelectron.* **2018**, *110*, 162−167.

(74) Jiang, Y.; Tan, C. Y.; Tan, S. Y.; Wong, M. S. F.; Chen, Y. F.; Zhang, L.; Yao, K.; Gan, S. K. E.; Verma, C.; Tan, Y.-J. SAW Sensor for Influenza A Virus Detection Enabled with Efficient Surface Functionalization. *Sens. Actuators, B* **2015**, *209*, 78−84.

(75) Lee, S. J.; Kwon, Y. S.; Lee, J.; Choi, E.-J.; Lee, C.-H.; Song, J.-Y.; Gu, M. B. Detection of VR-2332 Strain of Porcine Reproductive and Respiratory Syndrome Virus Type II Using an Aptamer-Based Sandwich-Type Assay. *Anal. Chem.* **2013**, *85* (1), 66−74.

(76) Sabaté del Río, J.; Henry, O. Y. F.; Jolly, P.; Ingber, D. E. An Antifouling Coating That Enables Affinity-Based Electrochemical Biosensing in Complex Biological Fluids. *Nat. Nanotechnol.* **2019**, *14* (12), 1143−1149.

(77) Zhang, Y.; Liu, Y.; Ren, B.; Zhang, D.; Xie, S.; Chang, Y.; Yang, J.; Wu, J.; Xu, L.; Zheng, J. Fundamentals and Applications of Zwitterionic Antifouling Polymers. *J. Phys. D: Appl. Phys.* **2019**, *52* (40), 403001.